

Evaluation of 3D Printed Foam Patterns for Hybrid Lost Foam Casting of A356 Alloy

K. Fedorov¹, G. Stoyanov², N. Sydorenko¹, C. R. Ravindran², K. Fayazbakhsh^{1*}

¹Department of Aerospace Engineering, Toronto Metropolitan University, Toronto, Ontario M5B2K3, Canada

²Mechanical and Industrial Engineering, Toronto Metropolitan University, Toronto, Ontario M5B2K3, Canada

*Corresponding author: kazem@torontomu.ca; Tel: (+1) 416-979-5000 ext. 556414; fax: (+1) 416-979-5056; <https://orcid.org/0000-0003-3963-8282>

Abstract

Lost Foam Casting (LFC) is an economical method of producing high-yield metal castings by evaporative decomposition of expanded polystyrene (EPS) patterns during pouring. The method can be used to cast intricate patterns such as manifolds, engine blocks with internal cavities, and other complex geometries. To make the EPS foam patterns, specialized molds and tooling must be machined, making this process economical only for high-volume production. The present research presents a Hybrid Lost Foam Casting (HLFC) process, which leverages 3D printing technology to manufacture light weight foam patterns using fused filament fabrication (FFF). Thin-walled plate patterns were 3D printed using a foaming polylactic acid (PLA) feedstock with a low-density infill, achieving a bulk pattern density of 0.044 g/cm³, twice that of traditional EPS foam. Aluminum alloy A356.2 was cast using foam PLA and EPS patterns of the same geometry, but under different combinations of casting parameters of traditional LFC. Tensile and microscopy samples were machined from the plates for comparative analysis of mechanical properties and microstructure. Yield strength was essentially equal for all samples averaging 96.7 MPa for EPS and 95.7 MPa for PLA-based castings. Additionally, a complex valve body pattern was 3D printed, laser-scanned, and cast for dimensional analysis. Over 90% of the valve body surface was observed to fall within a tolerance zone of ± 0.2 mm.

Keywords

Lost Foam Casting, Hybrid Lost Foam Casting, Polylactic Acid, Expanded Polystyrene, Fused Filament Fabrication.

Journal of Manufacturing Processes

<https://doi.org/10.1016/j.jmapro.2024.07.080>

Abbreviations

CBA Chemical blowing agent
CV Critical value
DSC Differential scanning calorimetry
EPS Expanded polystyrene
FFF Fused filament fabrication
LFC Lost foam casting
HLFC Hybrid lost foam casting
MNR Maximum normed residual
PBA Physical blowing agent
PLA Polylactic acid
PMMA Polymethyl methacrylate
Ra Roughness average
RIC Rapid investment casting
Sa Surface average
SDAS Secondary dendrite arm spacing
Str Texture aspect ratio

1. Introduction.

Conventional Lost Foam Casting (LFC) is a near net shape process that relies on a sacrificial foam pattern to form a mold space in a bed of unbonded sand. The foam pattern is removed by thermal decomposition, as molten alloy fills the space and replaces the lost pattern (Fig. 1 (b)-(d)), giving the name to this process. The unbonded sand is prevented from collapsing into the mold cavity by internal gas pressure of decomposing foam, metalostatic pressure of the molten alloy, and vacuum applied to the sand flask. After solidification, the resulting casting can precisely replicate the geometry and finest surface detail of the original pattern. The process is economical due to ease of forming molds with loose sand, which does not require manual compaction or binding agents. It also allows production of castings with complex internal geometries without using preformed cores as required for traditional sand and permanent mold casting. Good geometrical tolerances and surface finish are trademarks of this process [1].

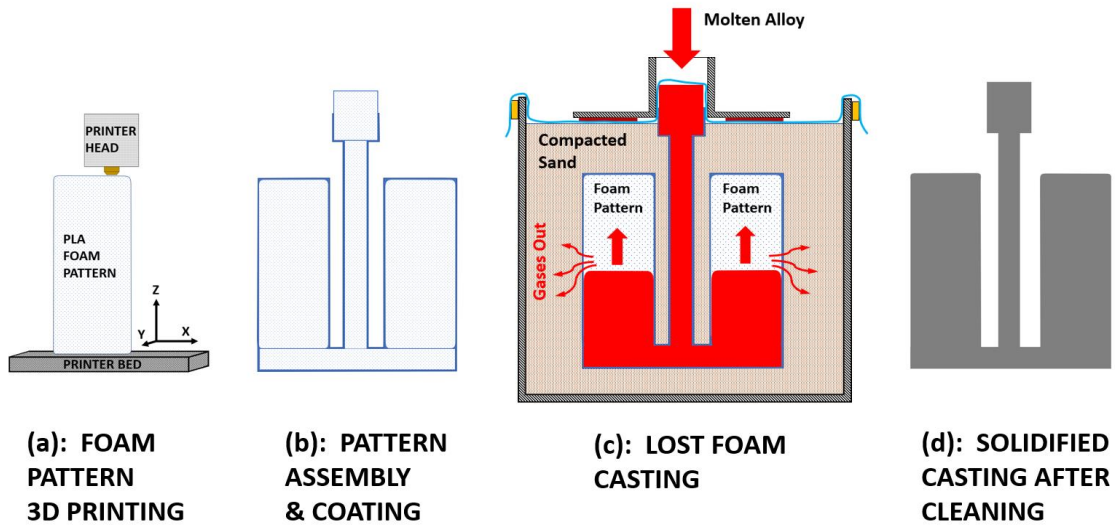


Fig. 1. Hybrid Lost Foam Casting process: (a) 3D printing of the foam pattern; (b) pattern assembly and ceramic coating; (c) direct casting of the pattern in a vacuum-assisted flask with compacted sand; and (d) resulting casting after solidification and cleaning.

The low-density foam pattern is traditionally made from Expanded Polystyrene (EPS). The pattern must be coated with a thin layer of a refractory ceramic prior to casting. The coating provides a barrier between the molten alloy and sand while also permitting EPS decomposition products to permeate through it. Without a coating, the molten alloy will infiltrate into the surrounding sand, producing a casting with a rough surface and inclusions [1, 2]. The unbonded sand must be compacted around the pattern with the assistance of vibration to prevent void defects. The pattern top is exposed and serves as an entry point for the molten metal. As the alloy is poured, the liquid and gaseous EPS foam residues escape the pattern cavity through the coating or float to the top through the pouring cup. Vacuum is usually applied to the sand flask to aid in the removal of liquid and gaseous foam byproducts.

The LFC foam pattern technology has been adopted from the packaging industry [2] that primarily uses EPS as the polymer of choice. The EPS foam pellets of polystyrene (PS) are subjected to the combined action of steam and pressure using specially machined molds. The EPS foam precursor pellets are infused with a blowing agent such as pentane, which enables them to expand when heated and form into foam. When the temperature reaches the glass transition point of PS, the blowing agent develops very fine gas pores within the pellets. As further heat is added, the pores expand until the pellets grow to over 20x of their original volume [3,4]. The expansion takes place until the beads come into contact and fuse together to form a foam pattern in the shape of a mold.

The main drawbacks of LFC are the initial cost and lead time to machine the tooling for the molding of EPS patterns, which will be factored into the final product cost. The process is only economical for high production volumes, where the initial investment in tooling can be justified. Complex geometries with internal cavities such as engine blocks, may require the final pattern to be assembled from smaller parts made in separate molds [2]. The foam parts must be joined with special assembly wax, adding to complexity (including higher heat of fusion) and production costs. Additionally, the widely available EPS foam technology has been primarily applied to aluminum and magnesium alloys and may not be suitable for metals with higher melting points such as steel and copper-based alloys. Higher melt temperatures

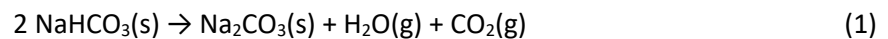
prohibit the use of EPS due to the tendency of PS to become pyrolyzed and leave traces of carbon in the solidified casting [2]. These alloys may require specialized foam materials such Polymethyl Methacrylate (PMMA), which are more challenging to make with existing methods [2].

Given the advantages and challenges of traditional LFC, the present research will investigate a Hybrid Lost Foam Casting (HLFC) Process that utilizes 3D printed foam patterns made by Fused Filament Fabrication (FFF). FFF is a rapid prototyping process based on extrusion of a molten polymer filament through a heated nozzle onto a base plate of the printer (Fig. 1 (a)). The motivation for this novel approach is the combined economy of manufacturing foam patterns by 3D printing and the minimal labor and resources involved with traditional LFC, post pattern-making stage. The ability to make foam patterns by 3D printing eliminates the need for specially machined tooling required in conventional LFC, reducing the lead time significantly. Consequently, the proposed HLFC process might become an option for low-volume and just-in-time production, which is currently not possible with LFC.

There are several alternative hybrid casting processes available such as Rapid Investment Casting (RIC) and 3D sand casting, both combining rapid prototyping technology with traditional casting. RIC is similar to the proposed HLFC in that a sacrificial pattern must be 3D printed but requires a multi-layer ceramic shell to be formed around the pattern prior to burnout [5]. The ceramic shell process is time consuming and demands specialized process control and materials [6,7], requiring the pattern to be burned out in a separate step before casting. After solidification, the ceramic shell removal can become difficult in undercut features and internal areas where the shell can be trapped. The rigidity of ceramic shell may create hot tearing defects during solidification. 3D sand casting is a relatively recent technique based on building of a mold from bonded-sand with a binder-jet printer [8]. While the 3D sand casting method excludes the need for the pattern burnout step, the volume of material that must be printed is significantly larger than in RIC or HLFC. The resulting sand mold must be printed in pieces that need to be cleaned, coated, and glued with a ceramic adhesive, leading to diminished tolerances and rough surface finish [8,9]. After casting, the leftover sand may not be reused due to binder residues.

The HLFC method has the potential benefits of a fast turnaround time, minimal consumption of materials, good surface finish and tolerances, ease of mold removal from the casting, and a reduction in hot tearing defects. Potential problems with HLFC are diminished mechanical properties of castings due to mixing of the flowing metal with the high-density 3D printed foam. The infill geometries of 3D printed patterns may encourage turbulent and inhomogeneous mixing of the alloy and polymer, leading to pyrolyzed carbon inclusions in the casting. Fillability of thin-walled features can also be more challenging than with other casting methods, along with common gas and carbon defects encountered in traditional LFC.

The most widely available foaming feedstock for FFF printers is polylactic acid (PLA) filament infused with a chemical blowing agent (CBA) such as sodium bicarbonate or a physical blowing agent (PBA) such as Thermally Expandable Microspheres (TEM) [10] and CO₂ gas. When heated above approximately 210 °C, sodium bicarbonate decomposes into sodium carbonate, water vapor, and carbon dioxide gas:



The quantity of gas formation is a function of heat applied to the filament as it passes through the printer nozzle. Slower extrusion rate and higher nozzle temperature provides more heat flow into the filament. The density of 3D printed foam is mainly controlled by these two variables. Current studies on 3D printed foam by FFF method involved changes to blowing agent concentration and adjustment of 3D printing variables as mentioned. There is no published literature indicating application of 3D printed foam to HLFC

or any similar casting process. Kalia et al. [10] varied the concentration of TEM-based blowing agent in a PLA filament to measure the impact on density, pore morphology, and mechanical properties of 3D printed foams. Higher concentration of blowing agent produced a decrease in foam density. Naguib et al. [11] showed that higher temperatures produced an increase in initial foam expansion followed by a collapse of the foam structure due to decreasing polymer viscosity at higher temperatures, while low temperatures did not generate sufficient gas expansion. An optimum temperature between the two extremes was found to produce the lowest foam density. Nofar et al. [12] provided a summary of current techniques employed to produce 3D printed foams with FFF method. In all cases studied, the lowest foam density and finest pore distribution were achieved with a balanced combination of blowing agent concentration, extrusion rate, and nozzle temperature. Marascio et al. [13] created a foaming PLA filament by infusion of supercritical CO₂ as a blowing agent. The process showed a potential to create low density foam with FFF method.

Pore nucleation in polymer foam occurs when the blowing agent gas pressure is sufficient to overcome the polymer's mechanical strength at elevated temperature. It must not be too high to cause the pores to coalesce and collapse the foam, and not too low to cause insufficient pore growth. Faster printing speed and extrusion rate will require higher nozzle temperature to transfer sufficient heat to the blowing agent. Examples of foam porosity for 3D printed foaming PLA and EPS foams are shown in Fig. 2. The 3D printed foam in Fig. 2 (b) shows the degree of foaming that can be achieved with commercially available foaming FFF feedstock compared to traditional EPS foam (Fig. 2 (a)). For PLA, a maximum pore volume of approximately 50% can be achieved with in-situ foaming [10] at the nozzle compared to over 95% pore volume of traditional EPS foams [3,14]. This limitation of foaming PLA in significantly reducing the pattern density can be overcome by reducing the infill density during 3D printing.

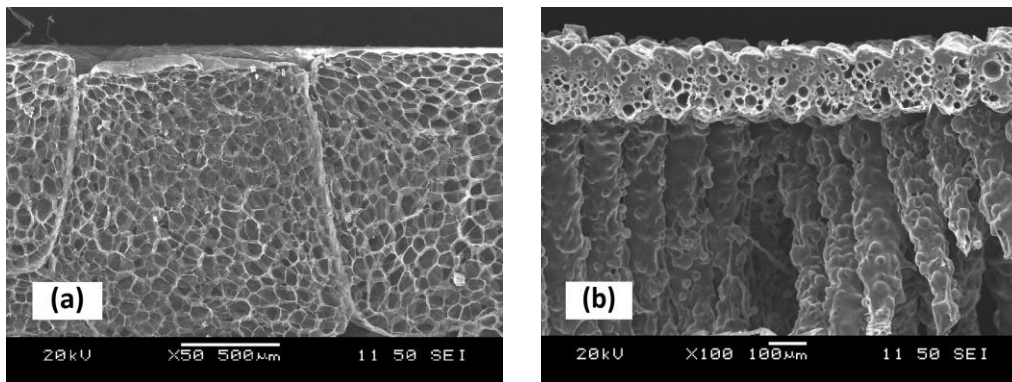


Fig. 2. SEM images of foam cross sections: (a) EPS foam, 0.02g/cm³ density; (b) 3D printed PLA showing the pattern edge and infill, eSUN LW PLA filament.

Existing research for conventional LFC metallurgy has been mainly focused on fillability, reduction of gas porosity, and carbon inclusions from EPS pyrolysis products. The challenge of traditional LFC is to combine the properties of low pattern density for low carbon content and high pattern rigidity for better dimensional tolerances. Lower density foam has less polymer mass that may leave carbon deposits in the casting. A popular model for molten alloy propagation through the evaporating foam pattern is illustrated in Fig. 3. The molten alloy is separated from the foam by a layer of gaseous foam byproducts and liquid PS. The gas and liquid are forced through the coating by metallostatic pressure, and the vacuum applied in the sand bed.

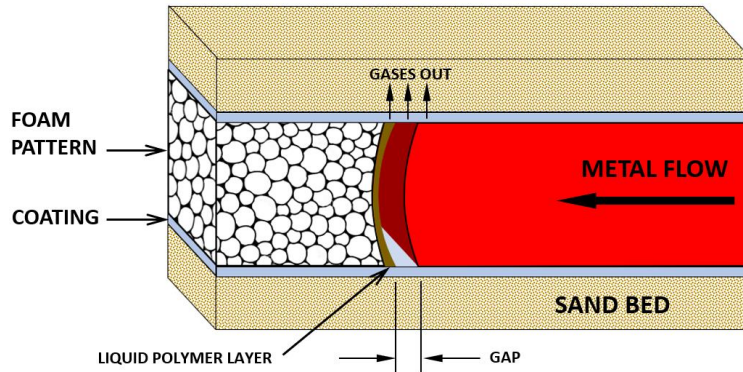


Fig. 3. Idealized model for advancement of the metal front through the pattern in LFC with a gap filling mode.

Fasoyinu and Griffin [15] investigated the impacts of melt temperature, vacuum, and pressure level, on the fillability of thin-walled patterns and tensile properties post heat treatment. Higher superheat (alloy temperature above liquidus temperature) produced better fillability of complex and thin-walled features. Higher externally-applied pressure and vacuum levels produced a significant reduction in casting porosity.

Barone and Caulk [16,17] created numerical simulation of LFC mold filling with a novel criterion for determining what type of mold filling mode will be dominant for a given geometry and flow direction. Four distinct modes of foam filling were identified: contact, gap, collapse, and engulfing. Contact mode assumes there is no vapor gap between the metal and foam; instead, a thin layer of molten PS separates the two. The resulting high-density liquid PS layer is pushed into the coating porosity as the metal displaces the foam. In the gap mode, foam decomposition vapors separate the metal from the liquid layer and foam (Fig. 3). The gap insulates the metal front and allows gaseous byproducts to escape into the sand. These two modes (contact and gap) dominate most LFC filling and were used by Barone and Caulk for numerical analysis. The simulations helped to explain the filling behavior that disagreed with existing numerical simulations which were based on simplified relationships such as:

$$q_F = h_F(T_M - T_F) = \rho_F \epsilon_F u \quad (2)$$

where q_F is the heat flow from the metal into the foam pattern, T_M and T_F are the initial temperatures of the liquid metal and foam, ρ_F is the foam density, ϵ_F is the foam thermal decomposition per unit mass, h_F is the heat transfer coefficient (empirical constant), while u is the metal front velocity. Such relationships do not consider variable flow velocities caused by coating permeability and the foam vaporization rate.

Ajdar et al. [18] demonstrated the applicability of Chvorinov's rule to LFC of A356 plate castings. Chvorinov's rule was originally developed for sand and permanent mold casting. The total solidification time is expressed by Chvorinov's rule [19] by:

$$t = C \left(\frac{V}{A} \right)^n \quad (3)$$

where A and V are surface area and volume of the casting, C is Chvorinov's constant dependent on the mold and alloy properties, while n is a constant that varies between 1 and 2 depending on the alloy. The volume to area ratio V/A is known as the modulus, signifying that thin plate castings with large area have

faster solidification times than the more spherical shapes of same volume. A theoretical relationship for the filling length in LFC was presented in the following relationship:

$$L_f = \frac{\rho_L v \alpha}{2 h_g (T_M - T_i)} \left(C_L \Delta T + \frac{H_L}{2} - \frac{H_E \rho_P}{\rho_L} \right) \quad (4)$$

Where ρ_L = density of molten alloy, v = flow velocity, α = plate thickness, h_g = heat transfer coefficient, T_M = melting temperature of alloy, T_i = ambient temperature, C_L = heat capacity of molten alloy, ΔT = superheat, H_L = latent heat of molten metal, H_E = decomposition energy of foam, ρ_P = density of foam pattern foam. All parameters in this relationship are easily determined except for flow velocity v , which must be measured experimentally. They measured flow velocities for different plate thicknesses by observing the flow of alloy within a heat resistant glass container.

The present research will combine current techniques to 3D print low-density PLA foam patterns for a novel HLFC process and evaluate their performance relative to traditional EPS patterns. The properties being analyzed are fillability, mechanical properties, surface roughness, and dimensional tolerances. The control variables are pattern material (PLA and EPS), superheat temperature, coating thickness, and filling direction. To authors' knowledge, no prior research exists on foam 3d printing as it pertains to LFC. The present study will be an attempt to amalgamate the two processes of foam 3D printing and LFC.

2. Experimental Procedure

To evaluate the properties of castings made with 3D printed PLA foam, a series of plate patterns were made along with EPS foam patterns of same dimensions. The basic pattern geometry was a flat plate 200 mm x 100 mm x 10 mm, attached to a runner assembly as illustrated in Fig. 4. A356.2 alloy was selected due to extensive research available for the LFC process and the wide application of this alloy in the automotive and aerospace industries [20]. The governing process variables were: foam type (3D printed PLA and standard EPS), pouring temperature (750 °C and 800 °C), refractory coating thickness (one and two coats), and filling direction (bottom-up and top-down filling), listed in Table 1. Melt superheat controls the energy contained in the alloy that can be used to decompose the foam before solidification. Coating thickness effects the gas dissipation rate and likewise impacts mold fillability. Filling direction determines the mode of polymer residue removal from the mold, either by wicking through the coating in the case of bottom-up filling or floating to the top for top-down filling. Once the castings were completed, the analyzed properties were fillability (measured as percentage of 200 mm plate length), as-cast tensile strength and elongation, density, and microstructure properties.

Table 1. HLFC Process parameters.

Process parameter	Value 1	Value 2
Pattern Material (density)	EPS Foam (0.021 g/cm ³)	PLA Foam (0.044 g/cm ³)
Pouring temperature	750 °C	800 °C
Coating thickness	1 coat	2 coats
Fill direction	bottom-up	top-down

A total of 8 castings (16 plates) were produced (Fig. 4). The sample thickness of 10 mm was chosen as this lies at the low end of the thickness range explored in the literature, which spans from under 10 mm to over 50 mm thick. Thinner pattern geometry is more challenging to fill due to higher modulus (surface area to volume ratio) and was therefore selected to explore the limits of fillability obtainable with 3D

printed PLA foam. The width and length of the plates are sufficiently large to fit three 8-inch flat tensile specimens per ASTM B557-15 [21] and one additional sample for micrography (Fig. 4 Center). After casting, each of the plate samples was cut into samples for tensile tests and microscopy. The microscopy samples were used for density measurement and analysis of microstructure, porosity, carbon inclusions, and surface roughness.

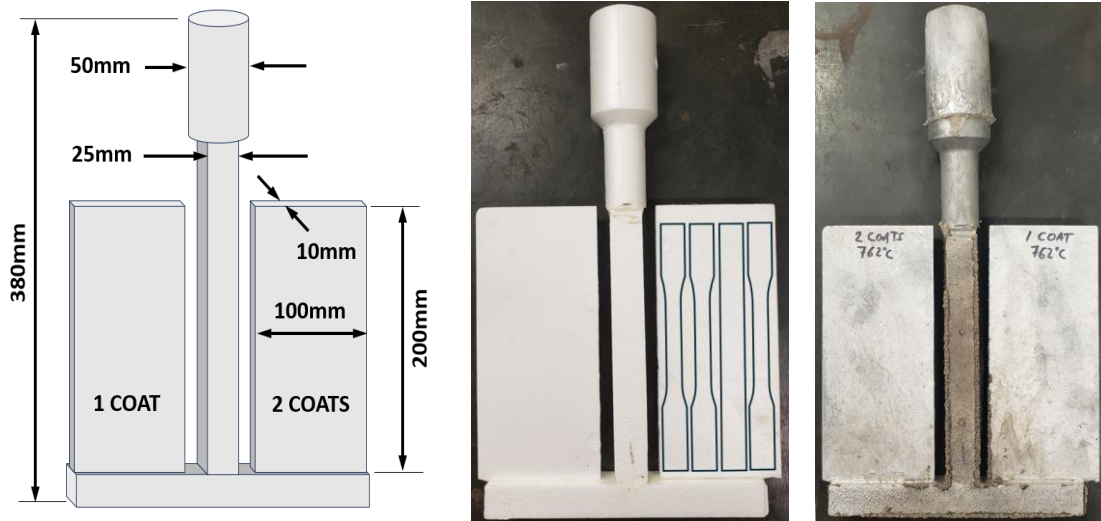


Fig. 4. LFC process for EPS pattern with bottom-up filling orientation: pattern dimensions (Left), EPS pattern assembly showing arrangement of tensile and microscopy samples (Center), and A356.2 alloy casting (Right), poured at 750 °C.

In addition to plate samples, a separate pattern was 3D printed for Geometric Dimensioning and Tolerancing (GD&T) analysis and to assess the quality and fillability obtainable for more complex geometries than flat plates. The geometry chosen was a butterfly valve body shown in Fig. 5. The shape provided both cylindrical and parallel features typically assessed in GD&T measurements. The foam pattern was prepared using same settings as for plate samples and coated with two layers of refractory ceramic. The PLA foam pattern was laser scanned with HandyScan 3D (Creaform Inc., Lévis, Canada) with an accuracy of 0.025 mm and 0.1 mm mesh. The resulting casting was scanned likewise and compared to the foam pattern using VXelements software. Casting for the valve body was performed in the top-down filling configuration.

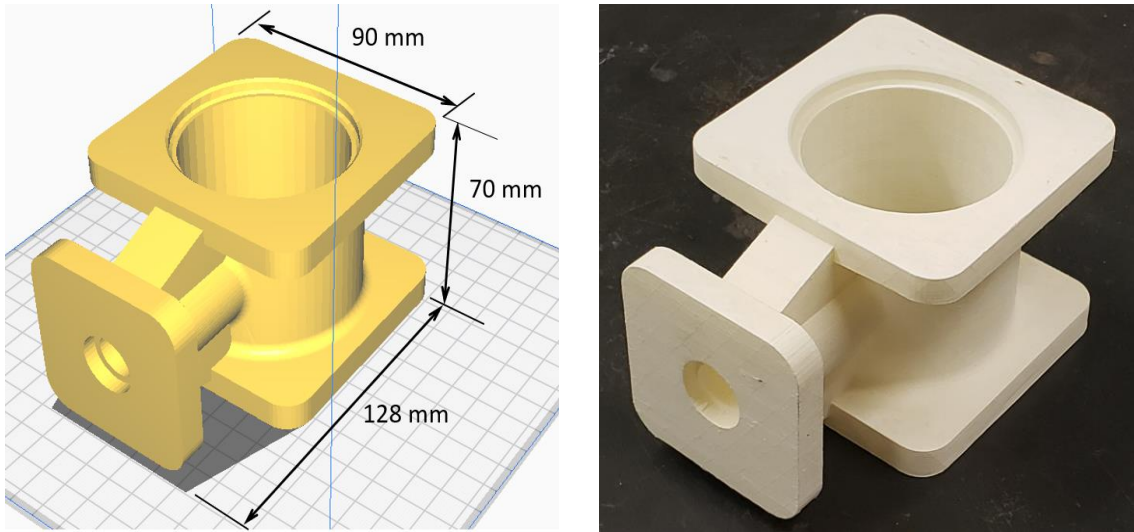


Fig. 5. HLFC butterfly valve body for GD&T analysis: 3D model (Left), 3D printed PLA pattern (Right).

2.1. Preparation of PLA and EPS Foam Patterns

The foaming PLA feedstock was a commercially available filament, eSUN Light-Weight PLA, 1.75 mm diameter, which uses sodium bicarbonate as the blowing agent. The 3D printer is a modified Anycubic model i3 Mega S FFF. The machine required an upgrade with a dual gear extruder equipped with a larger motor. This was necessary for the additional force needed to push the filament through a 0.2 mm diameter nozzle. All critical printing parameters are listed in Table 2.

Table 2. PLA foam 3D printing parameters.

Printer setting	Value	Printer setting	Value
Nozzle temperature	210 °C	Build plate temperature	40 °C
Printing speed	30 mm/s	Extrusion rate	40 %
Nozzle diameter	0.2 mm	Wall thickness	0.3 mm
Fan cooling	on	Top/bottom thickness	0.5 mm
Layer height	0.1 mm	Infill type	Cubic, 10 mm

The nozzle temperature and extrusion rate must remain constant to ensure consistent foam density. This applies to any foam extrusion process, whether 3D printing or industrial foam extrusion [4]. The printing process was therefore set up to have the same print speed for walls, infill, and support generation. Due to the low level of porosity obtainable with a foaming PLA feedstock, the only possible method to reduce overall foam density was by making use of a low-density infill pattern and a small wall thickness. Preliminary printing tests were conducted to find the lowest obtainable density with a combination of nozzle diameter, temperature, printing speed, and extrusion rate. Standard nozzle diameter of 0.4 mm produced an interrupted flow of foam when the extrudate width was reduced to 0.5 mm. The external diameter of this nozzle was producing tears within the pattern infill and wall exterior, possibly because of the ironing effect. The smallest diameter nozzle that could practically extrude the thin-walled foam was 0.2 mm. 3D printing speeds over 50 mm/s were found to produce tearing defects at all printing temperatures, possibly due to the foam having insufficient time to solidify as it was being deposited. The optimal printing temperature was determined by variation at a constant extrusion rate of 40%. Fig. 6 shows the printing process of the plates.

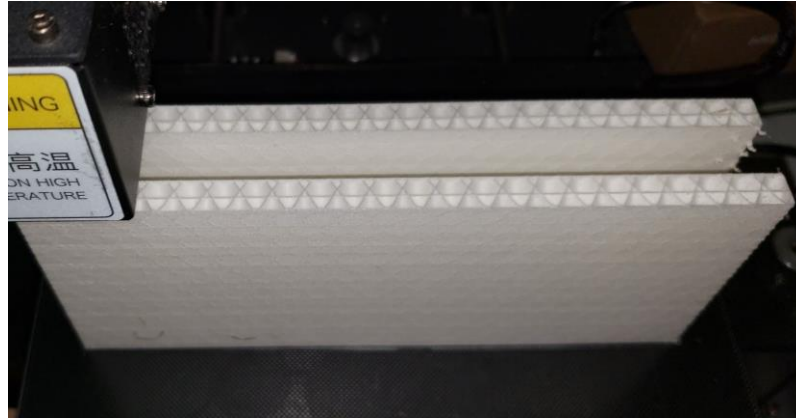


Fig. 6. 3D printing of the plate pattern in progress showing the infill geometry.

Using the printing parameters in Table 2, average density of 3D printed plates (200 x 100 x 10 mm) was 0.044 g/cm³ compared to 0.0215 g/cm³ measured for the EPS plate patterns. It must be noted that the foaming process in the 3D printed patterns only provides about 60% weight reduction compared to a regular PLA filament. Most of the density reduction is due to the large void ratio provided by the infill spacing of 10 mm (Fig. 7). Larger infill spacing was not used as it would make the pattern too fragile for subsequent operations. The foaming aspect of the 3D printed PLA pattern is an enabling factor that provides greater than 50% reduction of the bulk density. The GD&T pattern of the valve-body was measured to have a mass of 17.6 grams and a volume of 224 cm³, giving a bulk density of 0.078 g/cm³. The larger density resulted from a higher modulus of the valve geometry with more top/bottom surface area than in plate castings, which were printed vertically. The top and bottom surfaces require more print layers than walls.

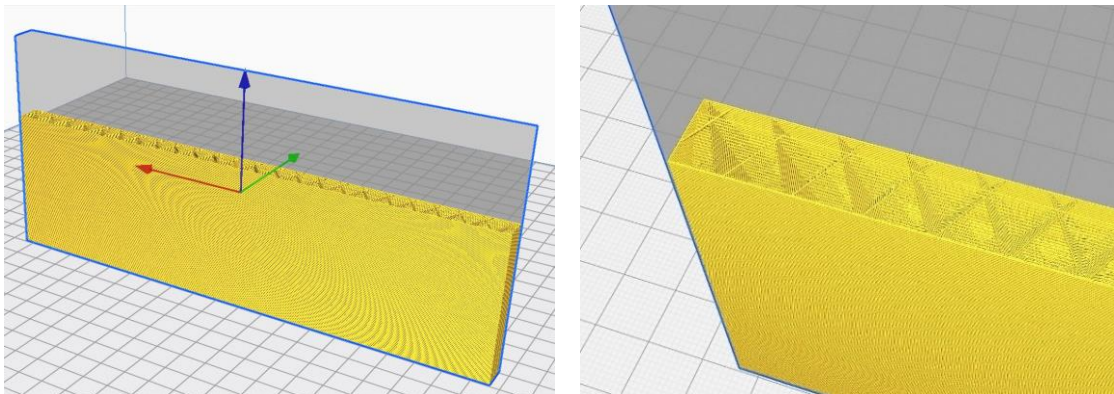


Fig. 7. 3D model of the plate pattern: model cross section (Left), closeup of the infill geometry (Right).

EPS foam patterns were prepared by cutting a 10 mm thick sheet from a larger stock with a hot wire saw. Both EPS and PLA patterns were then glued with LFC assembly wax onto gating and feeder assemblies prepared from EPS sheets (Fig. 4 Center). The feeders were 25 mm square in cross section and were connected to a cylinder that fitted snugly into the steel pouring cup. The overall assembly height and metallostatic head was 400 mm. Each assembly was coated with a single layer of a refractory coating (Ceramcote™ EP9, Ask Chemicals llc., USA) and allowed to dry. One of the plates was then coated

separately with a second layer. The coating was applied by manually submerging and soaking the pattern for 10 seconds, followed by a 5-minute drain time, during which the pattern was rotated for even distribution. According to the manufacturer's product sheet, the Ceramcote™ EP9 water-based, high-permeability coating comprises 20-30% Mica and 1-5% Quartz sand. Coating thickness was measured on average 0.77 mm for the first coat and 2.59 mm for the second. Thickness was measured on multiple points over the pattern before the coating and after the coatings were applied.

2.2. Casting Process

The general layout of the casting setup is shown in Fig. 8. The patterns were placed in a bed of mullite sand (AFS35 GFN) by gradually compacting around the pattern with vibration for 60 seconds. The top of the casting flask was sealed with a plastic film and rubber seals to maintain vacuum within the sand during casting. A vacuum gauge pressure of -12 psi was applied initially during the casting, which gradually fell to -5 psi as the metal flowed into the pattern cavity and remained at that level until solidification. Aluminum alloy A356.2 was heated to 760 °C and 810 °C in an electric resistance furnace (for 750 °C and 800 °C pouring temperatures, compensated for heat loss during the crucible transfer) then degassed with 0.025% hexachloroethane and skimmed. A total melt mass of 2.2 kg was used for each casting.

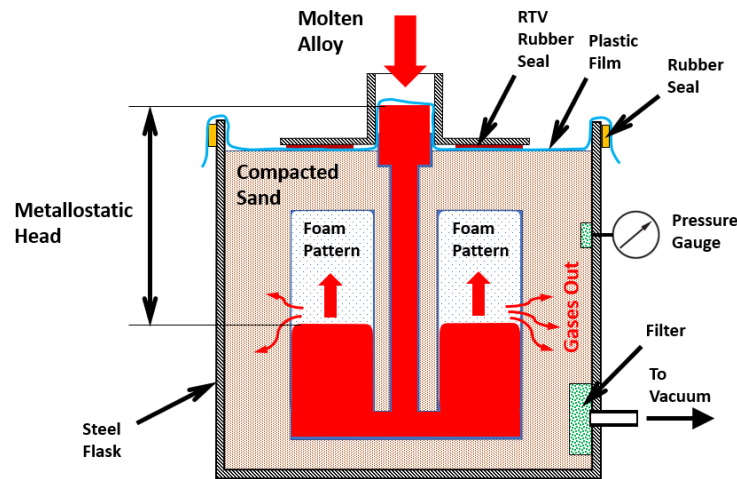


Fig. 8. Casting flask and pattern layout.

2.3. A356.2 Sample Preparation and measurements

After casting was completed (e.g., Fig. 4 Right), each plate was cut into 4 rectangular pieces, 3 of which were machined into tensile samples per ASTM 557B-15 (Fig. 9). Tensile testing was performed on a United Tensile Tester DTM 50 kN using 50 mm gauge length and an average sample thickness of 9 mm by 13 mm wide.

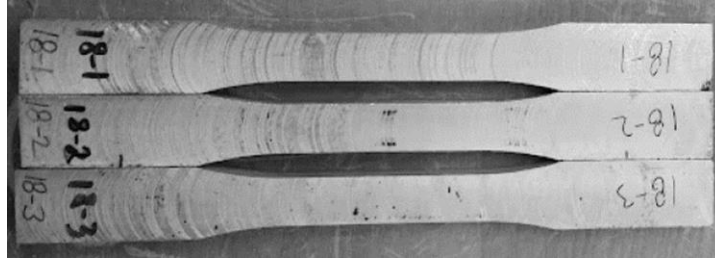


Fig. 9. Tensile samples machined from EPS-derived casting, 800 °C.

Density measurement was performed per ASTM B311 on the remaining pieces, then made into samples for microscopy, polished with 1 μm alumina followed by a 10% sodium hydroxide etch. Optical microscopy was carried out for microporosity measurement by image analysis, grain size and morphology, and carbon inclusions.







Surface roughness of castings from EPS and PLA patterns were measured with optical confocal profilometer Sensofar S Neox (Sensofar Metrology, Barcelona, Spain) at 1.38 μm resolution. EPS and PLA foam pattern surfaces were optically scanned on an area of 4 x 6 mm and three roughness parameters were measured with MountainsMap[®] software (Digital Surf, Besançon, France), roughness average Ra, surface average Sa, and texture aspect ratio Str. Both Ra and Sa parameters had a cutoff wavelength of 0.8 mm. Surface roughness of castings produced from EPS and PLA patterns were scanned likewise.

3. Results

3.1. Fillability

Fillability was 100% for all patterns except for bottom-up PLA foam castings, which filled to about 33% (Table 3). One plate sample from PLA foam (800 °C, single coat), filled approximately 40% of the plate. While pouring metal into PLA foam patterns, there was significant backpressure of the gas, causing portions of the metal in the pouring cup to spill out. This required the filling process to be interrupted for several seconds to allow the gases to dissipate. This was especially evident for top-down castings. All EPS patterns filled rapidly and without backpressure gas release.

Table 3. Fillability of EPS and PLA foam plate samples for all casting parameters.

Fill direction	BOTTOM-UP				TOP-DOWN			
	750 °C		800 °C		750 °C		800 °C	
	1 coat	2 coats	1 coat	2 coats	1 coat	2 coats	1 coat	2 coats
EPS Foam								



Portions of the pattern surface with one layer of refractory coating had melt infiltration into the surrounding sand, similar to that documented by Bichler et al. [2]. The defect was more pronounced on 800 °C castings due greater superheat energy that allowed the alloy to flow deeper into the sand before freezing. PLA plate patterns had minor infiltration defects at the corners (Fig. 10, red arrows) and none of the patterns had any infiltration on surfaces that had two coatings (Fig. 10). Corners of the patterns were more susceptible to infiltration defects than flat areas. Bottom-up castings for PLA foam patterns had significant surface carbon residue (Table 3). Top-down PLA foam castings had less surface carbon, which showed river-like carbon surface noted in past research [22].



Fig. 10. Melt infiltration and river surface, 750 °C, top-down filling: PLA foam casting (Left) and EPS foam casting (Right).

3.2. Mechanical Properties

Tensile measurements were performed only for top-down castings as PLA patterns did not fill completely for the bottom-up filling configuration. The Ultimate Tensile Strength (UTS) was higher for EPS foam than PLA in all castings, averaging approximately 139 MPa for all EPS-based samples versus 130 MPa for PLA (Fig. 11). Yield strength was essentially equal for all samples averaging 96.7 MPa for EPS and 95.7 MPa for PLA (Fig. 12). Average fracture strain for all EPS and PLA-based samples was 1.73% and 1.34% respectively (Fig. 13). The UTS and strain measurements for EPS-based samples showed higher values for 1-coat than 2-coat measurements. PLA-based castings showed larger variation in all UTS measurements compared to EPS. The Maximum Normed Residual (MNR) method was used to isolate outliers from the sample data with a Critical Value (CV) of 1.154. No outliers were detected due to the low CV value required for the small sample size of only three tensile specimens.

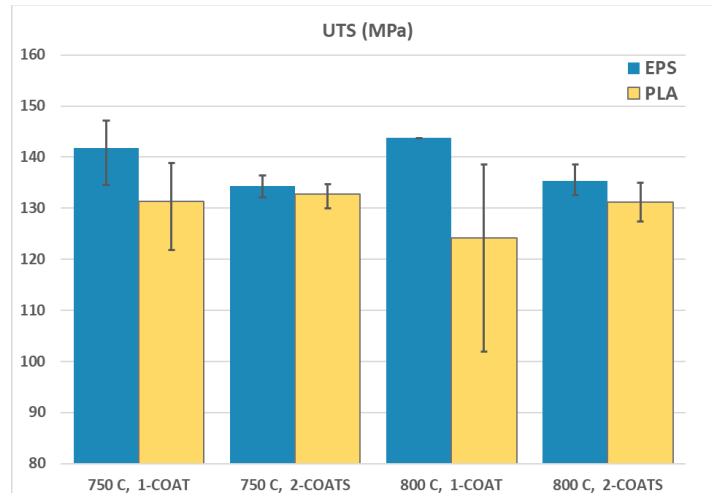


Fig. 11. Ultimate Tensile Strength for EPS and PLA top-down castings. Error bars represent minimum and maximum values.

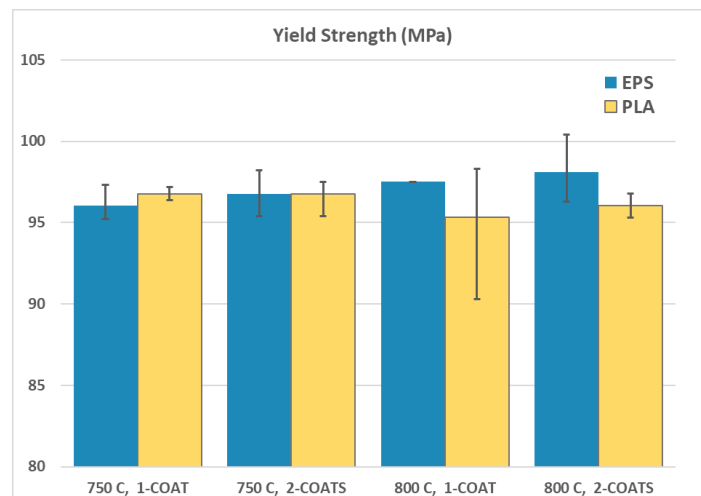


Fig. 12. Yield Strength for EPS and PLA top-down castings. Error bars represent minimum and maximum values.

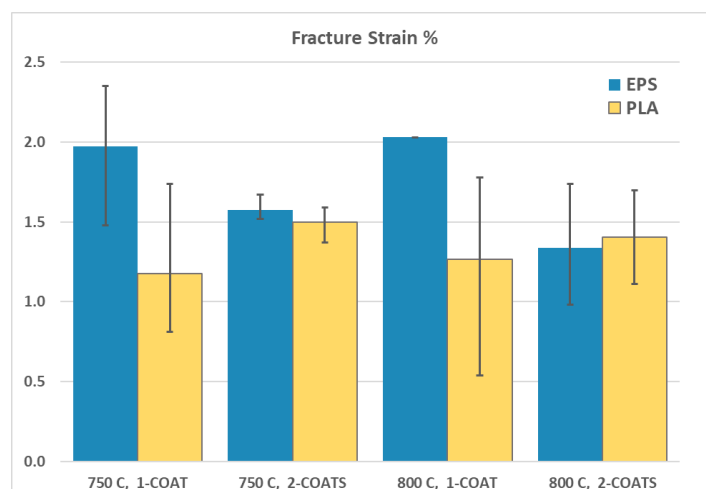


Fig. 13. Fracture strain for EPS and PLA top-down castings. Error bars represent minimum and maximum values.

3.3. Density Measurements and Microstructure

Fig. 14 shows typical porosity distribution along the interior of EPS and PLA-based castings after the samples were ground and polished. All respective EPS and PLA samples had similar porosity size and distribution with PLA showing larger pore size and number. Micrographs of EPS and PLA samples (1-coat, 800 °C) are shown in Fig. 15. Fold defects and carbon inclusions were observed in some PLA samples (Fig. 16).

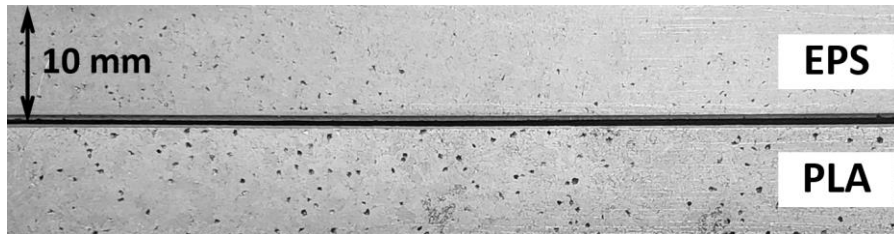


Fig. 14. Representative porosity distribution in A356.2 alloy samples for EPS and PLA patterns, 800 °C top-down casting, 1 coat.

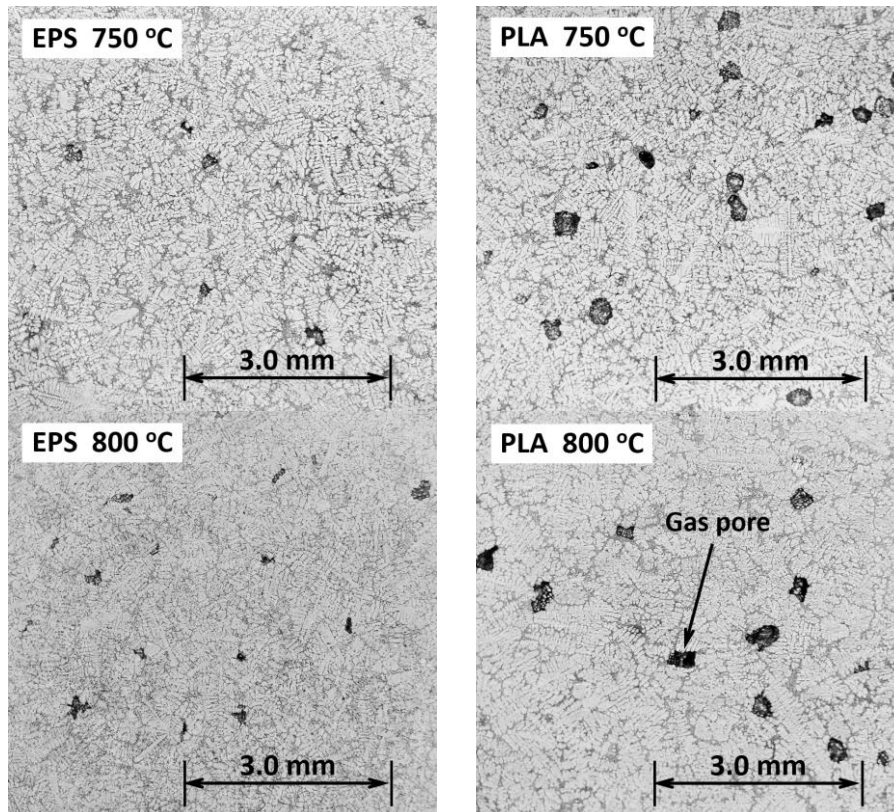


Fig. 15. Micrographs of A356.2 alloys samples from EPS and PLA-based top-down castings, single coat, showing alpha Aluminum and eutectic Silicon phases. Microporosity is more prominent in PLA-derived castings. Samples were polished with 1 μm Alumina and etched with 10% Sodium Hydroxide solution.

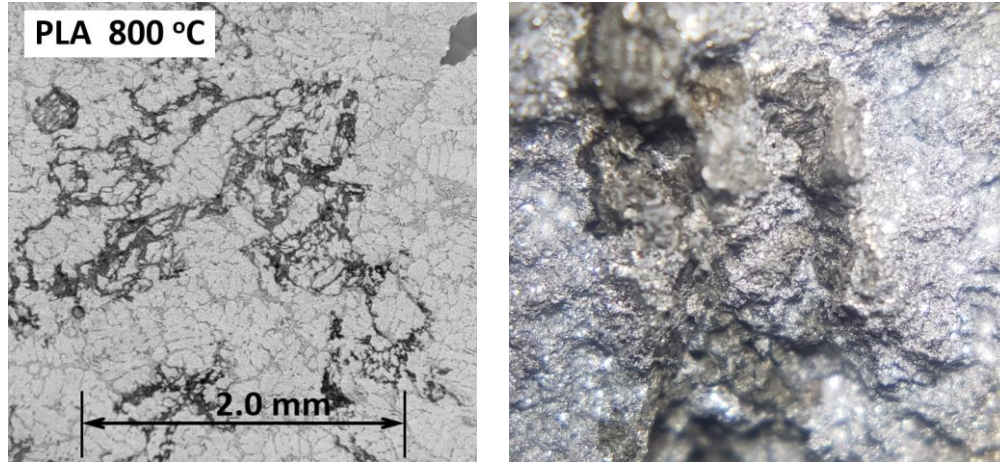


Fig. 16. Carbon inclusion in A356.2 alloy sample, PLA-based pattern casting, 800 °C top-down pour, 1 coat. Carbon inclusion as found in a micrograph (Left) and on the fracture surface of the same sample (Right).

Density measurements in Fig. 17 agree with porosity observations in the micrographs. EPS has a higher overall density of 2.62 g/cm³ versus 2.59 g/cm³ for PLA. Percent area density (Fig. 17 Right) was obtained by image analysis of micrographs by measuring the area occupied by the alloy relative to microporosity. Area density calculated using ImageJ software, shows a similar density distribution as obtained by the Archimedes method (Fig. 17 Left).

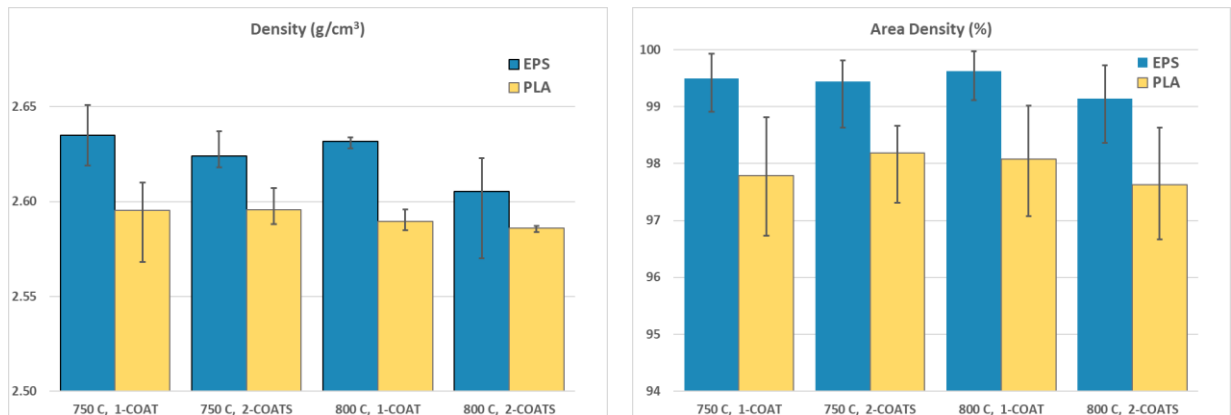


Fig. 17. Density measurements for EPS and PLA top-down castings obtained by Archimedes method (Left) and corresponding area density (Right) obtained by microporosity image analysis of micrographs (Area Density = 100% - porosity area). Error bars represent minimum and maximum values.

SEM images of fractured surfaces (Fig. 18) have the characteristic dimpled surface morphology that looks similar for both EPS and PLA. Interior porosity is more prominent in PLA than EPS-based samples.

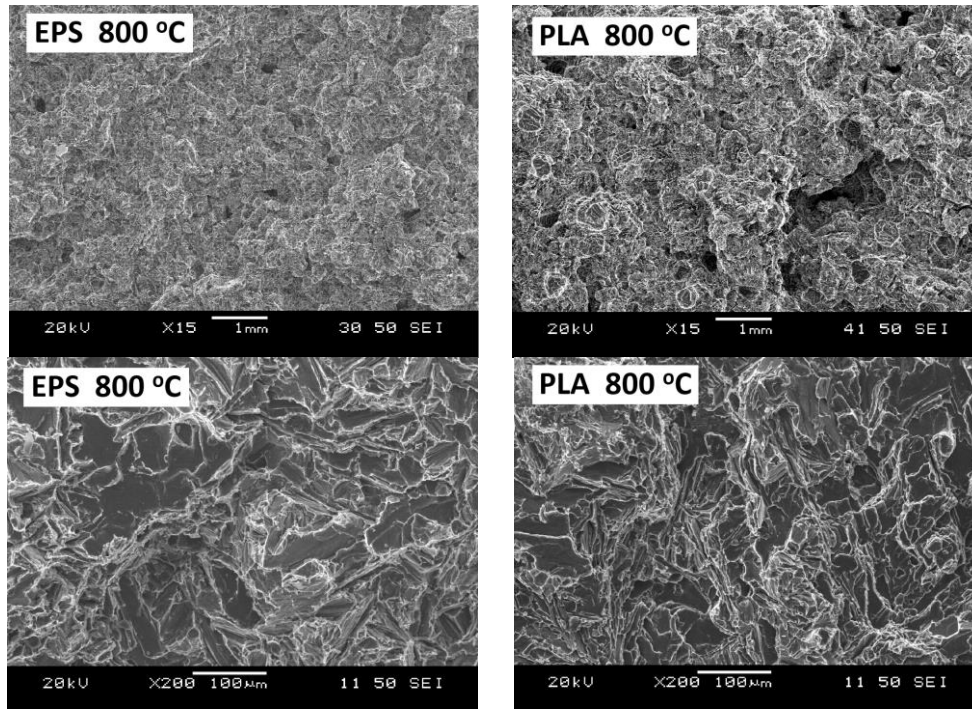


Fig. 18. SEM Fracture morphology A356.2 alloys samples from EPS (left) and PLA (right) patterns, 800 °C top-down casting, 1 coat. Interior porosity (top) is more prominent in PLA samples. Dimpled surface morphology (bottom) appears similar for both EPS and PLA.

Secondary Dendrite Arm Spacing (SDAS) was measured for each micrograph using ImageJ image analysis software. Overall, the SDAS for EPS was higher than PLA based castings due to the higher density of PLA foam and a faster resulting cooling rate of the alloy (Fig. 19). For all samples with two coats of ceramic the SDAS values were larger than single coat due to the higher insulative value of two coats and hence a slower cooling rate. Higher values of SDAS correspond to faster cooling rates.

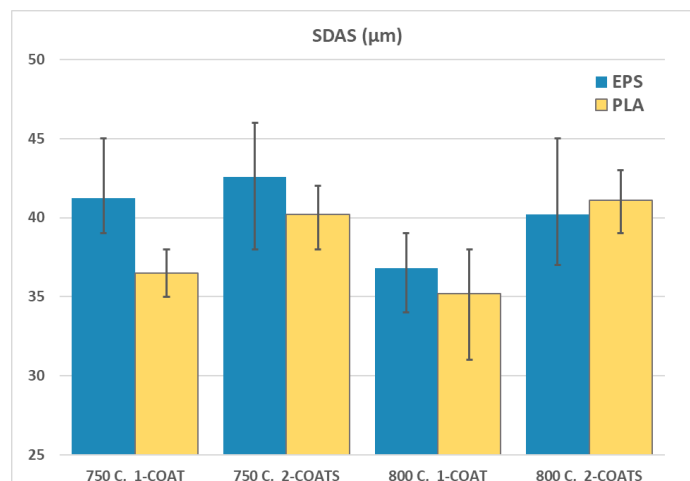


Fig. 19. Secondary Dendrite Arm Spacing measurements taken from micrograph samples. Error bars represent minimum and maximum values.

3.4. Surface Roughness & GD&T Casting

Surface Roughness scans for EPS pattern and casting at 750 °C are shown in Fig. 20, while those for PLA are shown in Fig. 21, both for 1 coat. EPS foam surface scan showed sharp edges where the foam beads pressed against the mold during EPS foam production. The resulting casting shows more rounded edges due to surface tension of liquid alloy [7] and some additional pitting is likely due to alloy solidification on the surface.

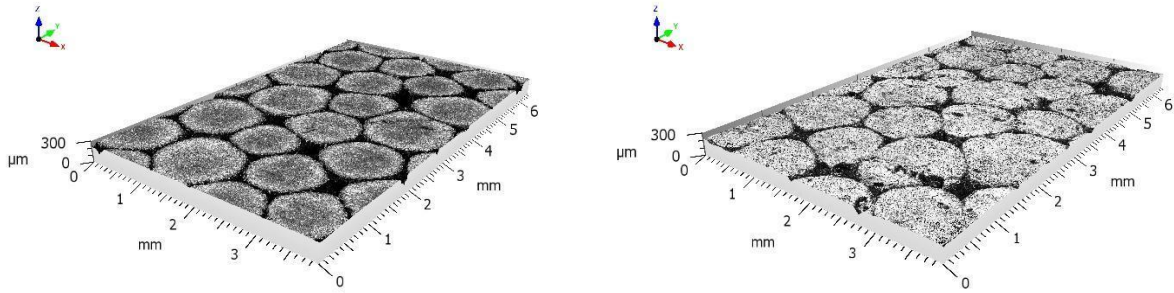


Fig. 20. Optical surface scans for roughness measurement: EPS pattern (Left) and resulting casting (Right) in A356.2 alloy, 750 °C, top-down, 1 coat.

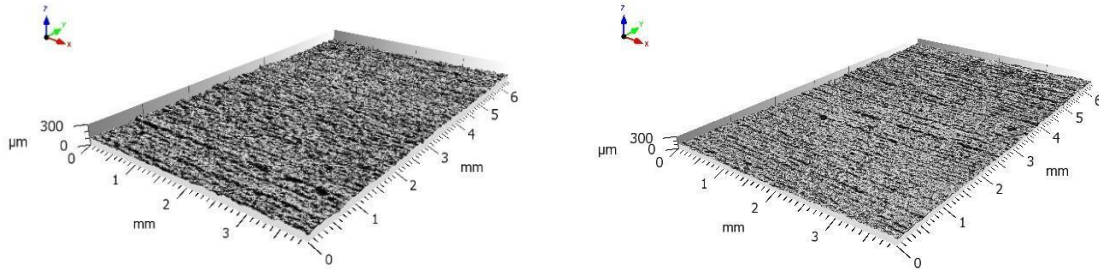


Fig. 21. Optical surface scans for roughness measurement: PLA foam pattern (Left) and resulting casting (Right) in A356.2 alloy, 750 °C, top-down, 1 coat.

The Ra, Sa, and Str roughness measurements are listed in Table 4. Sa is a surface roughness analog of the linear Ra roughness, and defined by the surface integral:

$$Sa = \frac{1}{A} \iint_A |z(x, y)| dx dy \quad (5)$$

where $z(x,y)$ represents deviation of each point from the mean surface. Str texture aspect ratio is a dimensionless roughness parameter that quantifies directionality or “lay” of surface texture. Surfaces with a roughness that does not depend on direction have Str values close to 1, while those with prominent directionality have Str close to 0. For 3D printed surfaces produced by FFF the directional stair-stepping roughness will have Str values close to 0 [6]. EPS foam and casting both had a uniform roughness and an Str of 0.87, while PLA foam pattern and casting has an Str value of 0.04.

Table 4. Roughness parameters (0.8 mm cutoff) for foam patterns and resulting castings at 750 °C.

Ra – Roughness Average		Sa – Surface Average		Str – Texture Aspect Ratio	
Pattern	Casting	Pattern	Casting	Pattern	Casting

EPS Foam	6.0 μm	4.9 μm	6.9 μm	8.8 μm	0.84	0.87
PLA Foam	8.1 μm	8.6 μm	8.9 μm	9.3 μm	0.04	0.04

The valve body casting (Fig. 22) was filled completely and likewise released gas from evaporating PLA foam during the filling process. The characteristic surface texture of 3D printing lines was clearly visible on the surface as plate castings, and no pitting defects were observed.



Fig. 22. GD&T (valve body) casting from 3D printed PLA foam pattern, 800 °C, top-down filling.

4. Discussion

4.1. Fillability

The difficulty of filling PLA foam patterns can be attributed to several known factors in the LFC industry. These are: coating permeability, pattern density, and thermal decomposition properties of the polymer. The dominant mode of foam removal from the pattern cavity is via transfer of liquid polymer through the porous ceramic coating. Hence, liquid polymer permeability is of main interest. The flow of fluid through a porous medium is governed by Darcy's law:

$$Q = \frac{k}{\mu L} \Delta P \quad (6)$$

Where Q is the volumetric flow rate, k is permeability of the coating, ΔP is the pressure difference across the coating, μ is kinematic viscosity of the liquid, and L is flow length (coating thickness). In the case of LFC, permeability is a function of coating surface wettability by the molten polymer and coating porosity. Kinematic viscosity μ of the molten polymer varies as a function of temperature. Polymers experience a gradual decrease of viscosity with increasing temperature above the glass transition point [23]. Higher melt superheat may therefore contribute to a decrease of viscosity and increased liquid flow rate through the coating. The pressure difference ΔP is a sum of vacuum pressure and metallostatic head. After initial flow of metal, the vacuum level dropped from -12 psig to -5psig (34500 Pa) as measured by the vacuum gauge and remained at the low level until complete filling. It should be noted that metallostatic head was increasing linearly to 400 mm in the case of top-down filling and decreased from 400 mm to approximately 175 mm for bottom-up filling. Maximum metallostatic pressure was therefore $P = \rho \cdot g \cdot h = (2370\text{kg/m}^3) \times (9.81\text{m/s}^2) \times 0.4\text{m} = 9300\text{ Pa}$ (1.35 psi). Maximum pressure acting across the ceramic coating was therefore $\Delta P = 34500\text{ Pa} + 9300\text{ Pa} = 43800\text{ Pa}$ (6.35 psi) for the top-down filling. For bottom-up filling $\Delta P = (2370\text{kg/m}^3) \times (9.81\text{m/s}^2) \times 0.175\text{m} + 34500\text{ Pa} = 36880\text{ Pa}$ (5.35 psi). Hence, vacuum level played a more prominent role in establishing ΔP than gravity for all castings in this experiment. Fillability in the case of bottom-up casting may be potentially improved for PLA-based patterns given that the vacuum level

remained at -5psig for the current experiment. In all existing research fillability has been directly linked to the vacuum level [15, 24-27]. Although excessive vacuum may be detrimental to casting quality for EPS pattern, the excess gas production of PLA-based patterns may be compensated in this manner.

In previous studies it was noted that wettability is a key factor in governing the flow rate of molten polymer through the coating [26, 27]. Non-wetting or hydrophobic surfaces will form a contact angle of more than 90 degrees, which greatly increases the pressure required to force the molten polymer through a porous medium [28]. Additionally, the contact angle formed by a liquid on a solid surface depends on the molecular polarity of the liquid. PS is a non-polar molecule consisting of a long chain of styrene monomers containing benzene rings, which lack any significant electronegativity between the constituent atoms [29]. PLA is a more polar molecule than PS and may therefore exhibit different wetting properties. Because the majority of refractory LFC coatings have been developed for PS, they may not be suitable for PLA in terms of wettability, in part because of polarity.

The kinematic viscosity of polymers μ , is a function of temperature. It is known that PS can remain in a liquid phase at temperatures well over 400 °C, with a progressively decreasing viscosity. The fact that PS remains in a liquid state at high temperatures may be responsible for the rapid removal from the mold cavity by wicking into the coating before evaporation and buildup of gas pressure occurs. The strong gas backpressure observed in PLA castings showed that PLA remained in the mold longer, due to lower permeability of the coating for liquid PLA and the fact that PLA patterns had twice as much polymer mass than EPS patterns.

Differential Scanning Calorimetry (DSC) tests performed on the eSUN PLA and EPS foam were performed up to a peak temperature of 400 °C with a heating rate of 20 °C/min (Fig. 23). The PLA foam exhibited all stages of pattern transformation within this temperature range from glass transition T_g , through crystallization T_c , melting T_f , and complete evaporation at approximately 380 °C. The EPS sample did not display prominent peaks on the DSC curve after T_g due to the lack of a distinct melting point notable of PS and a gradual evaporation of PS that takes place outside of the normal operating range of DSC. The ability of EPS to remain in a liquid state at higher temperatures, as evidenced by the DSC curve, allows the EPS pattern residues to wick through the coating more readily and without much evolution of gas.

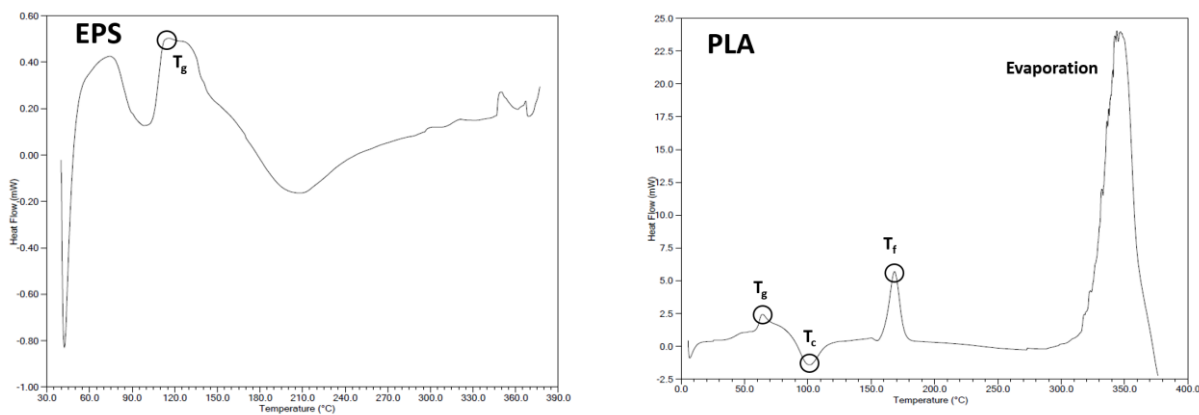


Fig. 23. DSC curves of EPS foam and eSUN foaming PLA after printing.

To demonstrate the differences in degradation properties of both polymers, DSC sample dishes were carefully opened to reveal the residues after the test (Fig. 24). The sample mass of EPS mostly remained

intact in a solidified form after melting. In contrast, the PLA sample has mostly evaporated. This supports what is seen in the DSC curves for both polymers.



Fig. 24. Residues inside DSC sample holders after the test. After the test, the EPS sample holder retains most of the polymer mass, while the PLA sample has degraded mainly by evaporation.

4.2. Mechanical Properties and Microstructure

The lower UTS and strain results for PLA-based castings are most likely related to the microporosity observed in micrographs and as confirmed by density measurements (Fig. 17) discussed earlier. Greater size and concentration of pores in PLA-based castings produced stress concentrations leading to a decrease of ductility and premature failure. The scatter observed for all PLA-based data is likely due to the random distribution of porosity, carbon inclusions, and fold defects (Fig. 16) observed in optical micrographs. The uniform yield strength across all samples is suggestive of similar base metal microstructure when porosity is not considered. Uniformly distributed pinhole porosity in the EPS based castings can be related to the relatively higher strength values compared to PLA based castings.

SEM images of the fractured surfaces show dimples that have similar morphology in both EPS and PLA-based samples. The dimples are indicative of a local ductile failure, which manifests as nearly identical yield strength values for all samples. The smaller SDAS observed in 800 °C castings relative to 750 °C is likely due to a faster cooling rate. The increase in SDAS observed for all 2-coat samples relative to 1-coat was due to a higher insulative value of 2 layers of ceramic coating, producing a slower cooling rate than 1-coat. Higher SDAS for EPS-based castings relative to PLA can be attributed to the greater density of PLA patterns and the resulting cooling rate of the alloy. Higher polymer mass consumes more thermal energy from the pattern, resulting in higher cooling rates.

The reduction in UTS seen in PLA relative to EPS-based castings can be partially accounted for by the reduction in load-bearing area caused by the larger porosity in PLA-based castings. The average difference in UTS between EPS and PLA-based casting for all samples is 6.44. While the corresponding differences for bulk and area density are 2.4% and 1.5%, with EPS-based castings having higher densities. Pore formation in castings is usually a product of solidification shrinkage and gas formation. Solidification shrinkage takes place during liquid-to-solid volume contraction, which is in the order of 5% for A356 [31]. As the liquid fraction decreases, the dendrite arms begin to interlock, blocking the passage of flowing metal in the casting interior. If the flow of feed metal is blocked, shrinkage pores will form between dendrite arms (Fig. 25). Local solidification parameters govern the degree of shrinkage. The dissolved hydrogen in the melt or LFC pattern residues will form gas porosity.

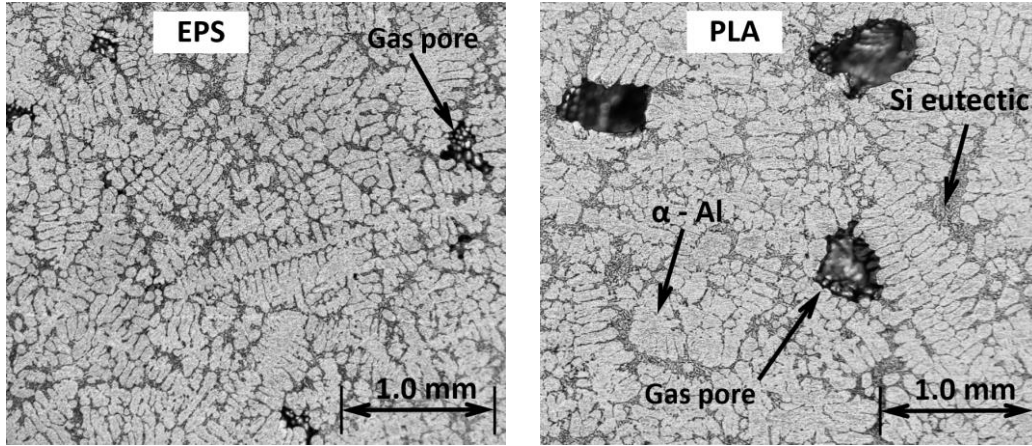


Fig. 25. Dendritic structure and porosity of A356.2 alloys samples from EPS and PLA-based top-down castings, 800 °C, single coat, showing alpha Aluminum and eutectic Silicon phases. The average pore size in PLA-based castings is significantly larger than EPS.

The growth of porosity during solidification is controlled by a balance of forces acting on the pore in a liquid metal [32] and expressed by:

$$P_g + \Delta P \geq P_{atm} + P_H + \sigma \left(\frac{1}{r_1} + \frac{1}{r_2} \right) \quad (7)$$

Where P_g is pore gas pressure, P_{atm} is atmospheric pressure, P_H is metallostatic pressure, ΔP is pressure from interdendritic flow, r_1 and r_2 are the principal radii of curvature of the pore, σ is the surface tension of the metal. The gas pressure from dissolved hydrogen in the melt will depend on the gas absorption and release level during the melting and degassing phases. Additionally, gas pressure may originate from decomposing LFC pattern debris suspended in the melt. A356 alloy initially solidifies in an alpha-Aluminum phase, pushing out the dissolved hydrogen and raising its local concentration in the interdendritic space [30, 32]. If the concentration exceeds the solubility limit, hydrogen will diffuse out of the melt into existing pores and inclusions present in the melt [30]. Subsequent growth of the gas pore will be governed by the balance of forces expressed in Eq. 7. Forces acting to minimize the pore diameter are external pressures due to atmospheric P_{atm} and metallostatic P_H heads, and surface tension of liquid alloy σ . Surface tension forces are strongest when the pore radius r is small, making it the dominant force during pore nucleation and initial growth. If solidification proceeds faster than the hydrogen diffusion rate, gas porosity may not occur or result solely from pattern degradation byproducts. The opposing forces favoring the expansion of the gas pore are the internal gas pressure P_g (from hydrogen or evaporating pattern debris) and liquid tensile stresses due to solidification shrinkage ΔP . Darcy's law can express negative pressure due to solidification shrinkage applied to solidification [32]:

$$\Delta P = \frac{\mu f_L \beta v_s}{K} l \quad (8)$$

Where μ is the kinematic viscosity of liquid metal, f_L is the liquid fraction, v_s is the feed metal flow velocity, l = length of fluid flow, $\beta = \beta' / (1 - \beta')$ and β' = solidification shrinkage, K is the permeability. In the case of solidification, the porous medium is a network of interlocking dendrites that block the passage of liquid to a given spot inside the casting. As solidification proceeds, the spaces between the dendrites (expressed by permeability K) become smaller, increasing the suction pressure that may lead to the formation of cavitation or gas pores. Higher hydrogen content or polymer residues will then aid in producing larger

pores that could otherwise form due to shrinkage alone. Severe gas porosity will produce spherical porosity in micrographs. Fig. 25 shows dendrite arms inside the pores resulting from both shrinkage and gas generation. Pore density for both EPS and PLA is approximately the same, while pore size is significantly larger in PLA-based castings due to excess polymer residues that could not escape the mold.

4.3. GD&T Casting

The valve body pattern was filled completely while having a minimum wall thickness of 4 mm in the cylindrical feature, less than half of the plate patterns. The overall valve body pattern density was 0.078 g/cm^3 , which is double that of plate patterns and four times the EPS foam density used in the experiments. The casting had fold and foam envelopment defects at the upper surfaces where molten foam residues floated and did not have sufficient time to escape before the alloy solidified (Fig. 16 & 26). The fold defect forms from thin graphitic films from two or more converging fronts of molten alloy. The film acts as a barrier and prevents the liquid fronts from mixing at a molecular level [30]. This type of defect typically forms at the top of last portions of the casting to be filled. The fold defects formed characteristic valleys on the surface contributing to the overall reduction in geometrical tolerance. As for plate castings, the overall surface roughness was a replica of the original pattern.

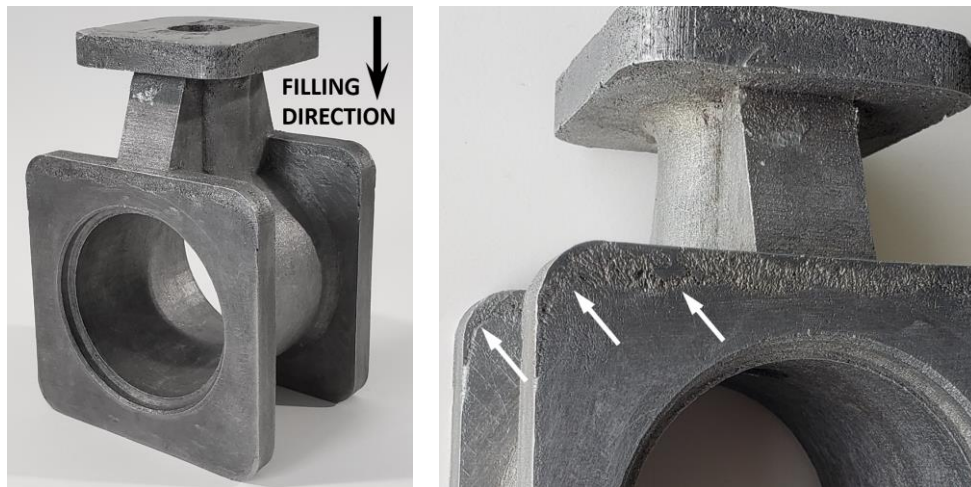


Fig. 26. Valve body casting showing fold defects from PLA residues after filling and solidification. White arrows indicating edge of the fold defect.

Laser scan comparison of the valve body casting and the PLA foam pattern showed that 45% of the valve body surface area was within $\pm 0.05 \text{ mm}$ tolerance zone from the 3D printed pattern, as marked by light green color in Fig. 27. The areas marked in dark red in the corners have likely resulted from excessive coating buildup in the negative corners of a pattern. Subsequent shrinkage of the thicker coating caused it to lift off from the pattern, producing a positive deviation. The areas marked in deep blue on the flange mostly originated from the machining operation for removing the runners connecting the valve body to the pouring cup. Over 90% of the valve body surface was within a tolerance zone of $\pm 0.20 \text{ mm}$, with the remaining deviations being due to excess coating material and the machining operation. The ridges due to fold defects were also visible on surface map but did not contribute significantly to overall surface deviation.

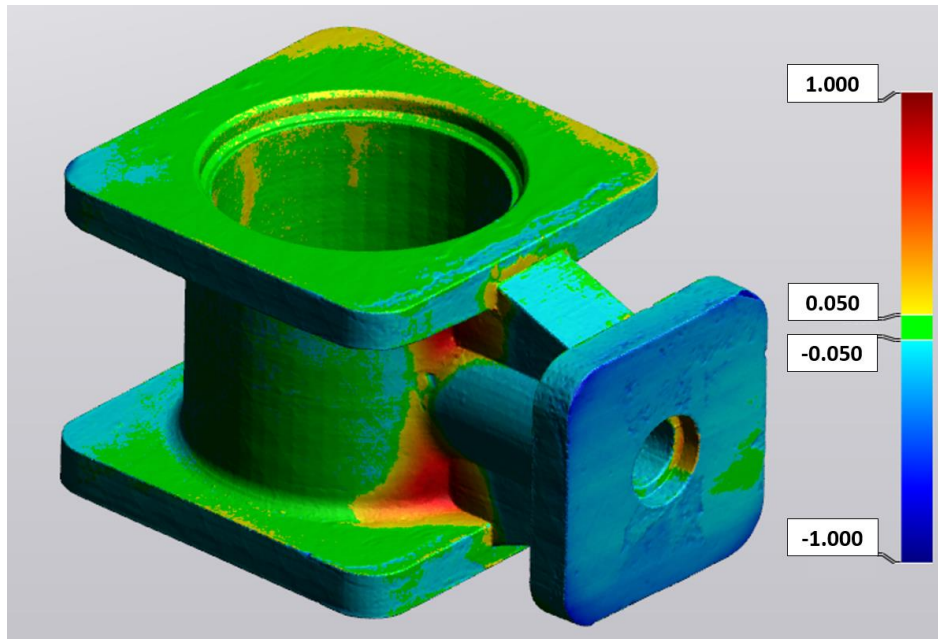


Fig. 27. Geometrical deviation between the laser scan of a PLA foam pattern and the resulting HLFC casting. Light green represents a tolerance zone of ± 0.05 mm. Upper and lower limits are ± 1.00 mm represented by deep red and blue on the color map.

4. Conclusions

The experiments demonstrated the possibilities of a novel HLFC process using a commercially available foaming PLA filament. The resulting castings were compared to traditional LFC samples made with EPS foam patterns. 3D printing parameters required for producing low density PLA foam patterns were provided. Fillability for PLA patterns was found to be limited due to the higher density of PLA foam and reduced permeability of refractory coatings for liquid PLA. Bottom up fillability for PLA foam was 30-40% for all superheats and coating thicknesses, while for EPS was 100%. For bottom-up casting PLA foam patterns showed strong gas release from the pouring cup but had filled completely, while EPS filling was equally smooth for both bottom-up and top-down orientations.

Yield strength was similar for all patterns castings, which suggests that base metal microstructure is unaffected by a PLA-based foam compared to EPS. Reduction of UTS and yield strength for PLA-based castings is caused by the higher porosity size and distribution left from PLA degradation byproducts confirmed by micrograph analysis.

Surface roughness of the GD&T casting and all other PLA castings except for bottom-up pattern, was slightly greater than that of EPS patterns due to stair stepping. The stair-stepping surface texture is inherent to any 3D printing process but can be minimized by smaller or variable layer thickness. GD&T pattern of a valve body with a minimum wall thickness of 4 mm and four times the density of EPS foam has filled completely in a top-down filling model. Fold defects were observed on the upper surfaces of the casting due to PLA residues being carried to the top by buoyant forces.

Aside from fillability and mechanical properties, it should be mentioned that the use of PLA patterns for HLFC is less harmful for the environment than EPS and poses a lower toxicity hazard due to the plant-based origins of the PLA precursor materials.

5. Further research

FFF method of 3D printing offers a variety of polymer materials that may be turned into foam with a suitable blowing agent. Polystyrene and PMMA filaments could be potentially infused with CBA or PBA type blowing agents to produce the desired foaming effect as was shown by Marascio et al. [13] with CO₂. PMMA foam has been used for higher melting ferrous alloys where PS poses a challenge due to pyrolysis residues [2]. In situ foaming PMMA filament feedstock may be created with a tuned combination of blowing agent, nozzle temperature, and extrusion rate to create foam patterns for ferrous alloys. Aside from PLA, PS, and PMMA, numerous other polymers may offer better performance in a HLFC process. Such polymers may also be made using a 3D printer based on a pellet extruder. Existing PS pellets used for foam production could be used to make 3D printed PS foam patterns. The pellets could be infused with pentane or CBA such as sodium bicarbonate or acetic acid. Specialized pellet extruders could be equipped with in situ addition of blowing agent such as CO₂ or N₂ to create low density foams with polymer types most suitable for a particular alloy. As was discussed in the present research, alternative ceramic coating materials may be explored for PLA and other polymers. Infill type and variable infill density may also be explored to improve the pattern rigidity and minimize mixing of polymer with metal.

FFF method of 3D printing offers a variety of polymer materials that may be turned into foam with a suitable blowing agent. PMMA filaments could be potentially infused with CBA or PBA type blowing agents to produce the desired foaming effect. In situ foaming PMMA filament feedstock may be created with a tuned combination of blowing agent, nozzle temperature, and extrusion rate to create foam patterns for ferrous alloys. Specialized pellet extruders could be equipped with in situ addition of blowing agent such as CO₂ or N₂ to create low density foams with polymer types most suitable for a particular alloy. Alternative ceramic coating materials may be explored for PLA and other polymers.

Acknowledgments

The authors thank Dr. M. Papini for the use of optical surface scanners for roughness analysis, Alan Machin for machining tensile specimens, and Dr. Raja Roy for reviewing the manuscript. We also acknowledge the financial support provided by the Natural Sciences and Engineering Research Council of Canada (NSERC), RGPIN-2023-04091 and RGPIN-2020-06096.

References:

- [1] Brown, J. ed., 2000. *Foseco ferrous foundryman's handbook*. Butterworth-Heinemann.
- [2] Bichler, L. and Ravindran, C., 2008. Effect of Foam Quality and Metallostatic Pressure on the Mode of Filling in A356 LFC. *AFS Trans*, 98, pp.955-956.
- [3] Jagoo, Satiendra (Uttam) (2007). Development of novel polystyrene composite beads for defect-free lost foam casting. Toronto Metropolitan University. M.A.Sc. Thesis. <https://doi.org/10.32920/ryerson.14646063.v1>
- [4] Reglero Ruiz, J.A., Vincent, M., Agassant, J.F., Sadik, T., Pillon, C. and Carrot, C., 2015. Polymer foaming with chemical blowing agents: Experiment and modeling. *Polymer Engineering & Science*, 55(9), pp.2018-2029.

- [5] Beeley, Peter R., and Robert F. Smart, eds. *Investment casting*. London: Institute of Materials, 1995.
- [6] Fedorov, K., Fayazbakhsh, K. and Ravindran, C., 2022. Surface roughness and dimensional tolerances in A319 alloy samples produced by rapid investment casting process based on fused filament fabrication. *The International Journal of Advanced Manufacturing Technology*, pp.1-15.
- [7] Fedorov, K., Ravindran, C. and Fayazbakhsh, K., 2023. Effects of process parameters on friability and surface quality in the rapid investment casting process. *The International Journal of Advanced Manufacturing Technology*, 125(1-2), pp.731-742.
- [8] Hodder, K.J. and Chalaturnyk, R.J., 2019. Bridging additive manufacturing and sand casting: Utilizing foundry sand. *Additive Manufacturing*, 28, pp.649-660.
- [9] Upadhyay, M., Sivarupan, T. and El Mansori, M., 2017. 3D printing for rapid sand casting—A review. *Journal of Manufacturing Processes*, 29, pp.211-220.
- [10] Kalia, K., Francoeur, B., Amirkhizi, A. and Ameli, A., 2022. In situ foam 3D printing of microcellular structures using material extrusion additive manufacturing. *ACS Applied Materials & Interfaces*, 14(19), pp.22454-22465.
- [11] Naguib, H.E., Park, C.B. and Reichelt, N., 2004. Fundamental foaming mechanisms governing the volume expansion of extruded polypropylene foams. *Journal of applied polymer science*, 91(4), pp.2661-2668.
- [12] Nofar, M., Utz, J., Geis, N., Altstädt, V. and Ruckdäschel, H., 2022. Foam 3D printing of thermoplastics: a symbiosis of additive manufacturing and foaming technology. *Advanced Science*, 9(11), p.2105701.
- [13] Marascio, M.G.M., Antons, J., Pioletti, D.P. and Bourban, P.E., 2017. 3D printing of polymers with hierarchical continuous porosity. *Advanced Materials Technologies*, 2(11), p.1700145.
- [14] Ho, S., Ravindran, C. and Hibbard, G.D., 2010. Magnesium alloy micro-truss materials. *Scripta Materialia*, 62(1), pp.21-24.
- [15] Fasoyinu, Y., Chiorean, H., Newcombe, P. and Sahoo, M., 2005. Vacuum Assisted Lost Foam Casting of Magnesium Alloy AZ91E. *AFS Transactions*, 113, pp. 887.
- [16] Barone, M. and Caulk, D., 2008. Analysis of mold filling in lost foam casting of aluminum: method. *International Journal of Metalcasting*, 2, pp.29-45.
- [17] Caulk, D., 2009. Analysis of mold filling in lost foam casting of aluminum: part II-example applications. *International Journal of Metalcasting*, 3, pp.7-25.
- [18] Ajdar, R., Ravindran, C. and McLean, A., 2002. Total Solidification Time and Flow Length of A 356 Alloy During Lost Foam Casting. In Transactions of the American Foundry Society and the One Hundred Sixth Annual Casting Congress (pp. 1497-1516).
- [19] Chvorinov, N., 1940. Theory of casting solidification. *Giesserei*, 27, pp.177-186.

- [20] Chen, Q. and Ravindran, C., 2000. A study of thermal parameters and interdendritic feeding in lost foam casting. *Journal of materials engineering and performance*, 9, pp.386-395.
- [21] ASTM International. Committee B07 on Light Metals and Alloys, 2015. Standard test methods for tension testing wrought and cast aluminum-and magnesium-alloy products (Metric). *ASTM International*.
- [22] Bichler, L. and Ravindran, C., 2006. Effect of Vacuum and Selected LFC Process Parameters on Mold Filling of AZ 91 E Castings: Part I-Casting Fillability and Surface Defects. *Transactions of the American Foundry Society*, Vol. 114, 114, pp.921-933.
- [23] Ainsworth, M.J., 2011. Metal-foam interface stability during the filling of lost foam moulds with aluminium alloys (Doctoral dissertation, University of Birmingham).
- [24] Jiang, W., Fan, Z., Liu, D., Dong, X., Wu, H. and Wang, H.S., 2012. Effects of process parameters on internal quality of castings during novel casting. *Materials and manufacturing processes*, 28(1), pp.48-55.
- [25] Jiang, W.M., Fan, Z.T., Liu, D.J., Liao, D.F., Zhao, Z., Dong, X.P. and Wu, H.B., 2012. Influence of process parameters on filling ability of A356 aluminium alloy in expendable pattern shell casting with vacuum and low pressure. *International Journal of Cast Metals Research*, 25(1), pp.47-52.
- [26] Sun, W., Littleton, H.E. and Bates, C.E., 2004. Advanced Lost Foam Casting Technology-Phase V. University of Alabama (US).
- [27] Bates, C.E., Littleton, H.E., Askeland, D., Griffin, J., Miller, B.A. and Sheldon, D.S., 1996. Advanced lost foam casting technology. 1995 summary report (No. DOE/ID/13230-T3). Univ. of Alabama, Birmingham, AL (United States).
- [28] Zhao, J., Kang, Q., Yao, J., Viswanathan, H., Pawar, R., Zhang, L. and Sun, H., 2018. The effect of wettability heterogeneity on relative permeability of two-phase flow in porous media: A lattice Boltzmann study. *Water Resources Research*, 54(2), pp.1295-1311.
- [29] Menczel, J.D. and Prime, R.B. eds., 2009. Thermal analysis of polymers.
- [30] Campbell, J., 2003. Castings. Elsevier.
- [31] Albonetti, R. and Ravindran, C., 1997. Effect of Adhesives on Microstructure of A356 Alloys in LFC (97-141). *Transactions of the American Foundrymen's Society*, 105, pp.609-620.
- [32] Chen, Q. and Ravindran, C., 2000. Effects of Hydrogen Content and Solidification Time on Porosity Formation in LFCs of A 356 Alloy- A Semi-Empirical Model. In *Transactions of the American Foundry Society and the One Hundred Fourth Annual Castings Congress* (pp. 297-303).